Article:
Goodall, A.D., Chechik, L. orcid.org/0000-0002-7626-2694, Mitchell, R.L. et al. (2 more authors) (2023) Cracking of soft magnetic FeSi to reduce eddy current losses in stator cores. Additive Manufacturing, 70. 103555. ISSN 2214-8604

https://doi.org/10.1016/j.addma.2023.103555

Additive Manufacturing 70 (2023) 103555

Contents lists available at ScienceDirect

Additive Manufacturing

journal homepage: www.elsevier.com/locate/addma

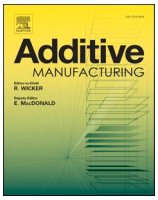

Cracking of soft magnetic FeSi to reduce eddy current losses in stator cores

Alexander D. Goodall [a,*], Lova Chechik [a], Ria L. Mitchell [a], Geraint W. Jewell [b], Iain Todd [a]

[a] Department of Materials Science and Engineering, University of Sheffield, Sheffield, UK
[b] Department of Electronic and Electrical Engineering, University of Sheffield, Sheffield, UK

ARTICLE INFO

Keywords:
Laser Powder Bed Fusion
Cracking
Soft magnetic material
Eddy currents
FeSi

ABSTRACT

To enable use of additively manufactured (AM) soft magnetic material in electric machines, large bulk cross-sections must be avoided as they allow large eddy currents, reducing efficiency. Fe-6.5 wt%Si is an excellent soft magnetic material, but is brittle. In this study we exploit this inherent characteristic of the material to develop crack networks within the AM material to inhibit parasitic eddy currents. By manipulating the laser parameters and scan strategy to purposefully induce cracking, the effective resistivity of the material can be increased to 206 μΩ·cm, 250% of the materials' already high resistivity of 82 μΩ·cm. Crack density is shown to increase with decreasing scan speed, and calculated electrical tortuosity shown to correlate with effective resistivity. Different scan strategies are shown to alter the orientation of the cracks, demonstrating that the crack orientation could be controlled in relation to the magnetic flux, providing high electrical resistance in the plane of the eddy currents, whilst maintaining magnetic properties. This method yields losses of 2.2 W/kg at 1 T, 50 Hz, similar to methods using air gaps, but with a much higher stacking factor of > 97%, outperforming other methods used in AM of soft magnetic material, showing promise for manufacturing stators of complex electric machines.

1. Introduction

Additive manufacturing (AM) has been revolutionary in enabling the manufacture of high performance and lightweight structural parts [1], allowing for topological optimisation, reduced component mass and material usage. Described as allowing high geometrical freedom [2], AM, however, has its drawbacks, including the occurrence of processing defects such as porosity and cracking [3]. Whilst this is undesirable in structural parts, these features may be beneficial in some instances, e.g. titanium orthopaedic implants, where high porosity facilitates bone ingrowth [4]. Other functional materials have received recent interest, such as soft magnetic materials, first additively manufactured by Zhang et al. [5]. Since this initial work, alloys such as Fe-Ni [6,7], and Fe-Co [8,9] have been successfully manufactured via AM to generate fully dense components.

Most research in soft magnetic materials focusses on Fe-Si [3,10–12], as this is the most commonly used soft magnetic material in industry. Silicon content is typically kept to < 3 wt% to allow the material to retain a degree of "workability" [13]. This allows rolling into thin sheets, known as electrical steel laminations, which when insulated and stacked upon each other, form the basis of most electrical machine (EM) stators. These laminations limit the eddy currents within the thickness of the lamination, decreasing losses. Higher silicon content electrical steel with 6.5 wt% rather than 3 wt% Si, has soft magnetic properties such as high permeability, high saturation magnetisation and low magnetostriction [14], making Fe-6.5 wt%Si a desirable material for use in electrical motors (EMS). However, it is difficult to process to form laminations by rolling as a result of the embrittling effect of the ordered phases (B2, D03) which form above 5 wt%Si.

AM has been shown to effectively process fully dense Fe-6.5 wt%Si [3] and the design freedom of AM could revolutionise EM design and manufacturing for More Electric Aircraft (MEA) [15]. However, to fully capitalise on the ability to additively manufacture this soft magnetic material, strategies must be implemented to reduce losses, specifically eddy current losses caused by large bulk cross-sectional areas in planes perpendicular to the magnetic flux pathway. AM affords the geometrical freedom to introduce thin air gaps between areas of deposited material. By using these air gaps as electrical insulators, the eddy currents can be confined to smaller cross-sectional areas, resulting in reduced eddy current losses. Plotkowski et al. showed that a Hilbert pattern can reduce losses to 1.34 W/kg at 1 T, 50 Hz [16]. Goll et al. [17] showed that a slotted pattern, similar to electrical steel laminations, could also reduce

* Corresponding author.
E-mail address: adgoodall1@sheffield.ac.uk (A.D. Goodall).

https://doi.org/10.1016/j.addma.2023.103555
Received 18 July 2022; Received in revised form 10 April 2023; Accepted 10 April 2023
Available online 11 April 2023

losses. Both of these methods use air gaps as electrical insulators, and other authors such as Koo et al. have processed air gaps to be as thin as 50 μm [18]. However, these often have unwanted shorting between adjacent sections as a result of the surface roughness, and still yield a low stacking factor (volume of magnetic material/total volume) of approximately 80 %. A stacking factor (SF) this low could impact upon the minimum size of an EM, an important selection parameter especially in the transportation and aerospace sector.

In this study the possibility of introducing stochastic cracking by manipulating process parameters is investigated. AM allows a level of control to spatially vary microstructure and processing parameters unavailable in many traditional processes. To allow the magnetic flux to run in three dimensions in an electric machine, it may be possible to tailor the orientation of the cracking within the material. This would yield the highest possible resistivity in the plane in which eddy currents will circulate, hence reducing the losses. This could give a spatially graded material with anisotropic effective resistivity, providing electrical machine designers unprecedented freedom over the magnetic flux pathways in the magnetic circuit, previously limited to 2D by electrical steel laminations or to materials with poorer properties such as soft magnetic composites (SMC).

These cracks would result in structures which limit eddy currents using cracks of 1–10 μm width, instead of designed air gaps approximately 100 μm, hence increasing the stacking factor. Scan strategy and laser parameters are manipulated to yield different crack patterns which can provide an advantage when orientated with respect to the magnetic flux path. The cracks are investigated using X-ray computed tomography (XCT) and the effective electrical resistivity is measured. Finally, a ring sample is used to compare the magnetic performance between bulk material, a purposefully cracked sample and a Hilbert cross-section (similar to Plotkowski et al. [16]), demonstrating that this is a promising method for processing soft magnetic material via AM.

2. Materials and methods

2.1. Sample processing

High silicon steel powder (Fe-6.5 wt%Si) supplied by Höganäs was used for all samples in this paper. The particle size and chemical composition, as stated by the supplier, are presented in Table 1, showing that the exact silicon content is lower, at 6.2 wt%. As a result of the atomisation process, the powder composition varies between batches; throughout this study, the alloy will be referred to as Fe-6.5 wt%Si to allow for comparison with literature.

This powder was processed using an AconityMINI (Aconity3D GmbH). This is a powder bed fusion - laser beam (PBF-LB) manufacturing system which employs a 200 W ytterbium doped continuous wave laser (wavelength 1074 nm) with a spot size of 70 μm. The PBF-LB process takes place under an argon atmosphere with an oxygen content < 100 ppm. The samples were built on a stainless-steel build platform of 140 mm diameter with a constant layer thickness (l) of 30 μm. Hatch spacing was kept at 100 μm for all experiments and the laser power used was 195 W in all cases excluding sample 1_ref, which uses a laser power of 170 W. The parameter set 1_ref had been previously found to give the highest density via a design of experiments methodology, which was used to optimise processing parameters for the manufacture of fully dense parts. Laser scanning speed (v) and scan strategy were the two main variables explored in this study. Laser parameters and scan strategies are listed in Table 2 and scan strategies employed are shown schematically in Fig. 1. All samples were removed from the build platform by wire electrical-discharge machining.

2.2. Metallographic and cracking characterisation

$25 \times 25 \times 4$ mm (X, Y, Z) cuboidal samples were built to understand how laser parameters and scan strategy affected crack density and crack orientation. These samples were sectioned, ground and polished using standard metallurgical techniques. Grinding was completed using P1200 and P2400 grit papers, following by polishing with 9 μm, 3 μm, 1 μm, 0.25 μm diamond suspensions sequentially with a final polishing step using MasterPolish, all supplied by Buehler. Optical micrographs were taken of the XY and XZ planes using an Olympus BX51 microscope in conjunction with Clemex Vision PE system.

Fig. 6 shows a typical cross-section taken in the XY plane for sample 2_300_B, it is evident that the cracking behaviour is complex and it is not possible to understand this from a single optical micrograph, hence XCT was used to gain a 3D understanding of the crack morphology through a larger volume. Samples of $20 \times 2 \times 2$ mm (X, Y, Z) were mounted on a sample holder and then scanned using a Zeiss Xradia 620 Versa X-ray microscope. X-rays were generated using a tungsten transmission target and collected on a CCD (charge coupled device) 16-bit 2000×2000 pixel detector. Rather than scanning the whole sample, a region of interest with a field of view $\approx 2 \times 2 \times 2$ mm was scanned using the $4 \times$ objective, resulting in a spatial resolution of 1.9 μm. An accelerating voltage of 110 kV, and a source power of 15.5 W were used, a filter (HE6) was inserted to reduce unwanted lower energy X-rays which can create scan artefacts. 1601 projection images were collected per sample with a 2 s exposure time selected to reduce noise and improve scan quality. Scans were reconstructed with a voxel (isotropic 3D pixel) resolution of 2.76 μm. A filtered back projection method was used to reconstruct the data, and reconstructed .txm volumes were converted to 8-bit greyscale image stacks (.tiff) using Zeiss Reconstructor software.

Tiff stacks of approximately 1000 images were analysed using the batch solver in ImageJ [19] in both the XY plane and the XZ plane. The ImageJ macro rotated the tiff to obtain the correct orientation in relation to the build direction, cropped to the area of interest and auto-thresholded using the 'Triangle' method [20]. The analyse particles function was used, where particles with area smaller than 10 pixels and a circularity of greater than 0.5 were removed to reduce noise and exclude porosity and the remaining particles analysed. Using an

Table 2
Sample processing parameters and scan strategy.

Sample ID = ID_laserspeed_scanstrategy	Scan speed (mm/s)	Scan strategy	Inter-layer rotation (degrees)
1_ref (optimum bulk parameters)	700	B (Bidirectional)	67
2_300_B	300	B	0
3_400_B	400	B	0
4_600_B	600	B	0
5_800_B	800	B	0
6_400_BR	400	BR (Bidirectional with rotation)	90
7_400_S	400	S (Stripe)	0
8_400_SR	400	SR (Stripe with rotation)	90

Table 1
Fe-6.5 wt%Si powder details.

Chemical composition (wt%)						Size distribution (μm)			
Iron	Silicon	Oxygen	Nitrogen	Carbon	Sulphur	D10	D50	D90	D99
93.735	6.200	0.036	0.016	0.010	0.003	15.67	25.72	42.07	57.23

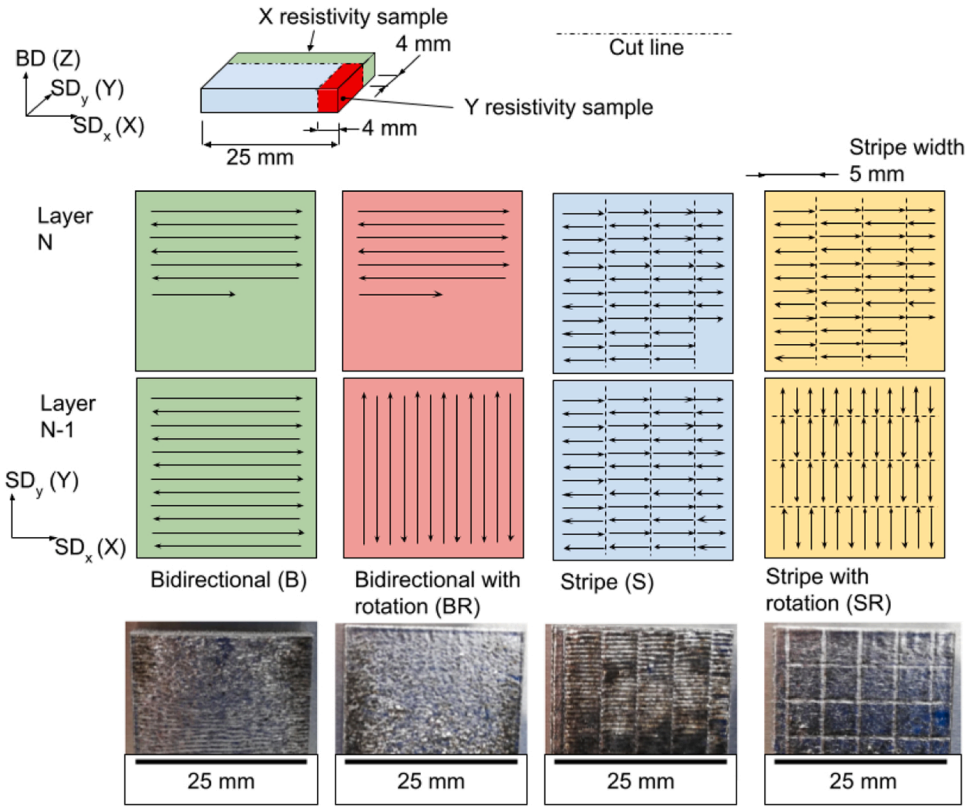

Fig. 1. Sample size shown along with X and Y resistivity samples, and scan strategies used in this study which include scan strategies that do not have any layer rotation, such as bidirectional (B) and stripe (S), along with scan strategies with a 90° layer rotation such as bidirectional with rotation (BR) and stripe with rotation (SR). Stripe width was kept constant at 5 mm in this study. Below each strategy is shown the sample resulting from that scan strategy with a scan speed of 400 mm/s.

automatic process ensures greater consistency between samples than manual thresholding. The outlines of these particles were saved as tiff images and a small sample of these were compared with the original tiff images to ensure that only cracks are recorded, not porosity or other features. Once all 1000 images were processed, the data for each of these particles is saved, which includes the orientation of a best fit ellipse and the Feret length, which were taken as approximations of crack orientation and length respectively. These data sets were processed using MATLAB R2020a [21] to calculate the crack density and orientation, which was separated into 5° bins. These data sets have between 20,000 and 80,000 values. An example of this workflow is shown in Fig. 2. The error in the crack density values was obtained by manually thresholding the image and obtaining crack data from a random image, repeating this 5 times and then calculating standard error. This error value is used for all crack density values given. For each image, crack density was calculated as the total length of cracks divided by the image area.

Electrical conductivity and tortuosity have been shown to correlate in porous materials [22], often used in the geotechnical industry to measure the conductivity of a pore network filled with a fluid. Tortuosity can be calculated using several different methodologies [23], where usually the pore space is the conducting medium. In this study Avizo 3D [24] is used to calculate the electrical tortuosity where the solid medium, which is the Fe-6.5 wt%Si, is the conducting medium and the crack and pore space is assumed to be perfectly insulating.

The tiff stacks are imported and cropped to remove the empty space in the scan. The end of sample edges display beam hardening and are removed to improve segmentation. Following this, a median filter was applied, the solid material segmented from the cracks/pores and a formation factor experiment used to investigate the electrical conductivity. The formation factor experiment imposes a potential difference at each

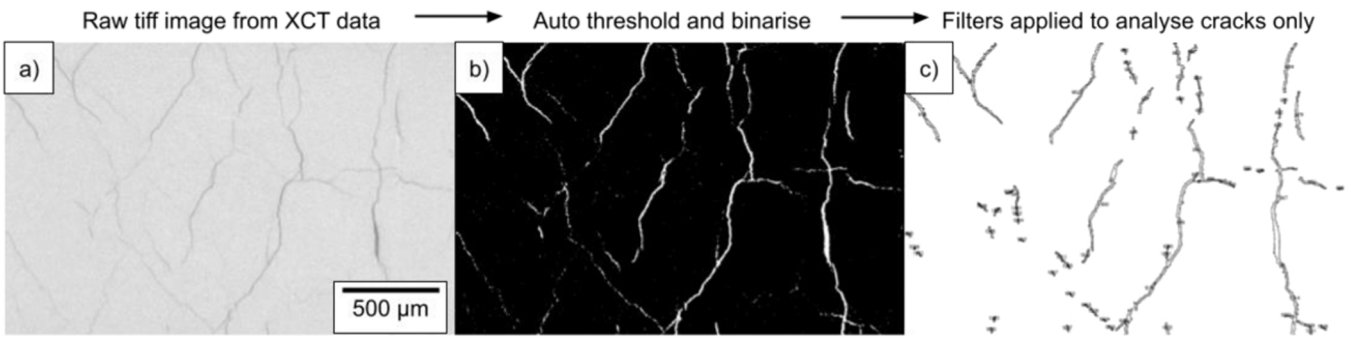

Fig. 2. Crack analysis workflow showing the cropped image from the XCT data (a), the auto-thresholded and binarised image (b), and the outlines of the particles analysed by ImageJ (c). This shows that only cracks are identified but that the total cracks are underestimated as some faint cracks are not identified, and some larger cracks have their length underestimated.

end of the sample, whilst the surfaces parallel to the current flow have a 1 voxel thickness insulator added to the outside as shown in Fig. 3. Using Ohms Law and conservation of charge averaged over a volumetric area, it is possible to calculate a formation factor which is "directly linked with the electrical conductivity through its inverse: the electrical resistivity" [25]. Further details of the calculation can be found in the Avizo user guide [25]. Using the result of this formation factor experiment, electrical tortuosity was calculated using a plugin [26] that defines electrical tortuosity as shown in Eq. (1), where F = formation factor and φ = Volume Fraction of Pore space. Tortuosity is a measure that describes a ratio between actual flow path length to the straight distance between the ends of the sample, as shown in Fig. 3.

$$\tau = \sqrt{F\varphi} \tag{1}$$

2.3. EBSD data collection and processing

EBSD (electron backscatter diffraction) samples were prepared by sectioning and polishing in the YZ plane to enable observation perpendicular to the scan tracks in the B scan strategy. The microscope used was an 7900F field emission gun (FEG) SEM manufactured by JEOL, fitted with an Oxford Instruments Symmetry EBSD detector, used with a 20 kV accelerating voltage and step size of 1 μm. The samples were mounted on the SEM stub using silver paste. AZtec by Oxford Instruments was used to capture and process the EBSD data, indexing the FeSi samples using the default parameters for α-iron, (BCC). The index rate was over 98 % for all samples inspected. Following the data acquisition, AZtec was used to align the EBSD map which has multiple frames, before exporting to.crc file format.

Analysis of EBSD data was performed in MATLAB R 2020a using the MTEX toolbox plugin. The data was imported and aligned to the coordinate system of the base plate to allow the data to be compared between samples. Then high angle grain boundaries were identified (> 10°), orientation maps and pole figures were plotted to visualise the data. Orientation maps were plotted in the XY plane, although the samples were inspected and are displayed in the YZ plane.

2.4. Resistivity and magnetic characterisation

Further segments were sectioned from the larger cuboid to obtain samples suitable for resistivity testing. The X-resistivity samples were approximately 25 × 4 × 4 mm (X, Y, Z) and the Y-resistivity samples approximately 4 × 20 × 4 mm (X, Y, Z) as per Fig. 1. A digital calliper was used to measure the length and cross-sectional area, which was taken as the average of the cross-section measured at each end. The resistance of these samples was measured 5 times using a Cropico DO5000 microhmmeter by Seaward, reversing the polarity after 3 measures, and converted to resistivity using Eq. (2), where ρ = resistivity, R = resistance, A = area and L = length.

$$\rho = \frac{RA}{L} \tag{2}$$

Throughout this paper, effective resistivity is used rather than absolute resistivity, as intrinsic material properties are not being stated, but rather the measured value from the cracked material. This value has been expressed through this paper as a percentage of the bulk resistance (82 μΩ·cm) as measured in this study and also reported in literature [14]. 5 samples were taken from sample 1_ref and the resistivity measurements repeated; the standard error was calculated and this value of error is used for all effective resistivity's.

BH loops and loss behaviour were measured using a toroidal sample of 30 mm inner diameter, 38 mm outer diameter, and approximately 4 mm thickness, respecting sample dimensions in BS 60404-4:2018 [27]. The cross-section of the ring was measured in three places using a digital calliper and the average taken; the mass was measured using laboratory scales. These toroidal rings were tested using an AMH-1K Permeameter by Laboratorio Elettrofisico controlled using Neon software, which calculates the density based on the cross-sectional area and mass. There is a 1 % tolerance on form factor of the measured sinusoidal B response, with a 2 % error on B measurements, a 2 % error on H measurements and a 3 % error on loss measurements. A thermocouple was used on the surface of the sample to ensure the temperature didn't increase above 40 °C. The rings were first wound with a single insulating layer of Kapton tape, then wound with 45 turns on the secondary search coil using 0.35 mm diameter single core copper wire and 40 turns on the primary coil using 1.5 mm diameter multi core wire. The specific power losses are calculated as per Eq. (3), where P_l = power losses, A = cycle area, f = frequency and ρ = density which is calculated using the cross-sectional area and mass.

$$P_l = \frac{A \times f}{\rho} \tag{3}$$

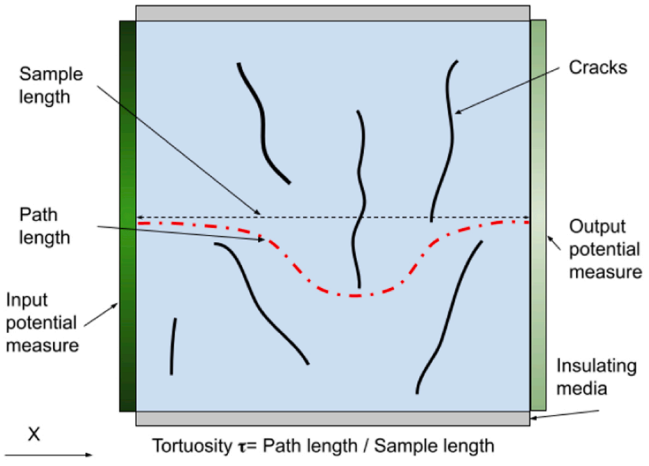

Fig. 3. Schematic showing tortuosity calculation, the path which must travel around the cracks within the sample. A potential is imposed at the input and output, whilst an insulating wall of 1 voxel thickness is applied at the surfaces parallel to the current direction (X).

3. Results and discussion

3.1. Effects of scan strategy and scan speed on resistivity

By changing the scan speed whilst keeping laser power, hatch spacing and scan strategy constant (sample 2–5), it is possible to observe that the slower the scan speed, the higher the crack density (Fig. 4). It is well known that excessive energy input can cause cracking in AM parts of certain alloys [28], however, as the tendency is to eliminate cracking from parts, there has been little study on the crack density variation with processing conditions. The limited data from this study shows a trend for lower scan speeds to increase the crack density, but the nature of this relationship is not fully understood. It is likely that there is a lower limit for scan speed at which parts will not build successfully as a result of excessive build defects, and a higher limit at which cracking no longer occurs and eventually, the samples will exhibit lack of fusion (LOF) defects. By altering the scan strategy, there is also an impact on crack density. By adding a 90° inter-layer rotation, as with scan strategies BR and SR, the crack density is elevated when compared to the B and S strategies.

Higher crack densities would give more opportunity for electron scattering when passing an electrical current, however as shown in Fig. 5, there is not a simple relationship between crack density and effective resistivity. For samples with the bidirectional scan strategy (B), it would appear that higher crack density yields a higher effective resistivity, although one of the samples with high scan speed (5_800_B) shows a higher resistivity than 4_600_B despite a lower crack density.

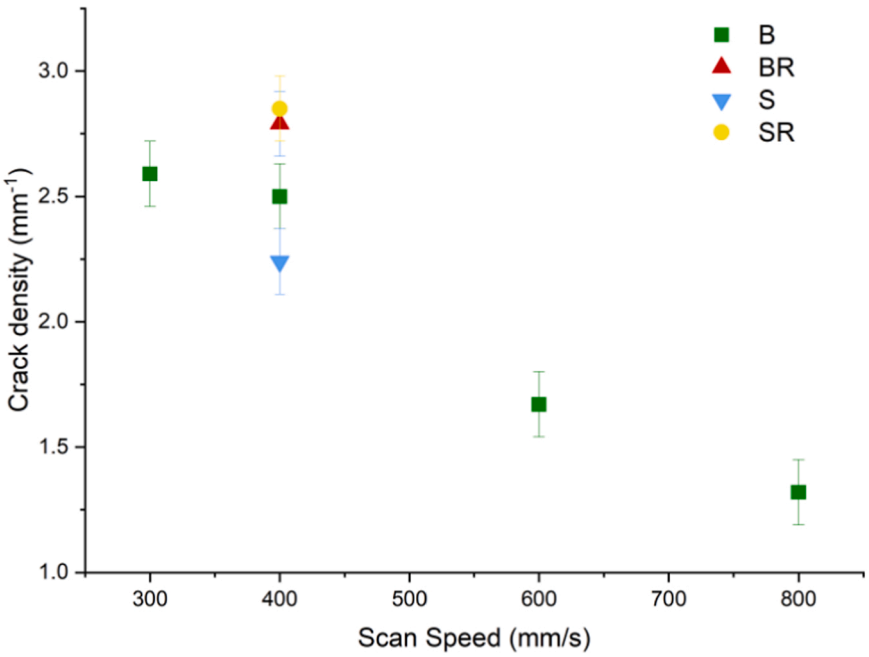

Fig. 4. Scan speed vs crack density showing that the slower the scan speed, the higher the crack density within the sample. It is likely at higher scan speeds cracking will stop as LOF starts to become apparent. At scan speeds lower than 300 mm/s heavy balling occurs, and the samples are not built successfully. By changing the scan strategy whilst maintaining scan speed, there is an effect on the crack density within the samples.

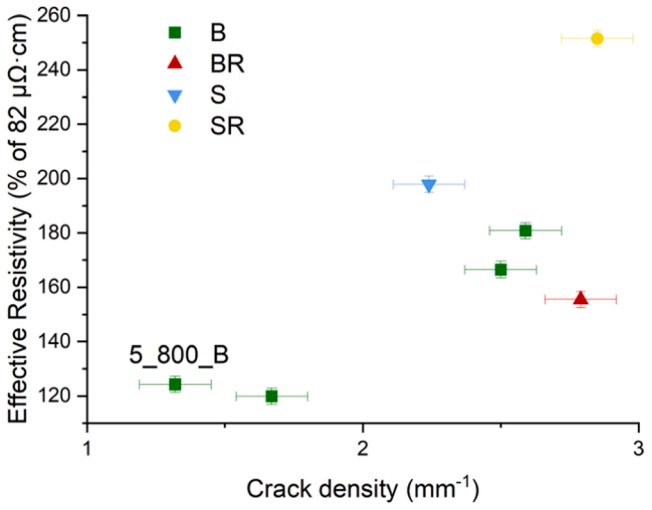

Fig. 5. Plot of effective resistivity against crack density, generally the more cracks a sample has, the higher the effective resistivity. The sample at the highest scan speed (5_800_B) exhibited both cracking and LOF defects which may explain why the first data point has a higher resistivity than the second, even though it showed a lower crack density.

Upon further investigation, it was found that sample 5_800_B had a number of LOF defects (Fig. 6), which are likely to increase the effective resistivity whilst not being accounted for in the value for crack density. The sample with the S scan strategy exhibits relatively high effective resistivity (≈ 200%) whilst having a lower crack density than some samples with lower effective resistivity. Based on this analysis, it is clear that crack density alone cannot predict the observed changes in electrical resistance.

As crack orientation varies significantly between samples, investigating a 2D cross-section cannot infer the crack distribution through the sample. It is not possible from such images, to tell the depth or changing paths of the cracks, so XCT was used to enable the crack networks to be viewed and analysed in 3D. The XCT data was obtained with sufficient resolution to facilitate the segmentation of the cracks and pores from the solid material, whilst maintaining the largest field of view possible. Using the XCT data, the electrical tortuosity was calculated in Avizo 3D for the same direction as the physical measurements (X), which considers not only crack density, morphology and orientation but also how the cracks are connected to each other. Calculated electrical tortuosity shows a linear relationship with the effective resistivity, as shown in Fig. 7.

3.2. *Effects of scan strategy on crack orientation*

Scan strategy B scans the material in the same direction within each layer. As residual stress has been shown to be higher normal to the scan direction [29], it is expected that cracks would occur normal to the scan direction as well. This would yield a higher tortuosity in the scan direction (X) than the perpendicular (Y) direction, as most cracks would align with current flow in the Y direction, giving a lower tortuosity. Therefore, for samples 2–5, where the scan direction is restricted to the X direction, cracks would increase the electrical tortuosity more for electrical current running in the X direction than the Y direction. To investigate this, samples were taken from both the X and Y direction and their effective resistivity measured as displayed in Fig. 8. As predicted, this shows that for bidirectional hatching, the effective resistivity in the X direction is significantly higher than that in the Y direction. Hence, if the eddy currents are generated in the XZ plane they would experience higher resistivity than if they were in the YZ plane. In this way it is possible to tailor the anisotropy of the material based upon the electric machine design, to ensure the highest level of resistance in the plane in which eddy currents generate. The orientation of these cracks is shown in Fig. 9, demonstrating that in the XY plane, the cracks are mostly orientated between 45° and 135° from the X direction, whereas in the XZ plane, the orientation of the cracks is centred at 90° from the X direction, but with a decreased variability.

By adding a layer rotation of 90°, sample 6_400_BR shows a decrease in anisotropy between the effective resistivity in the X and Y samples, demonstrating that the anisotropy can be preferentially selected using

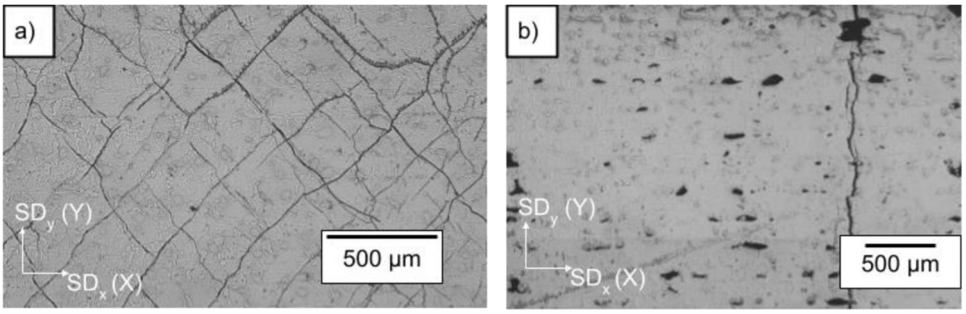

Fig. 6. Optical micrograph of 2_300_B sample (a) XY plane showing that the cracking shows a distinct pattern with the cracks running in preferred directions of 45° and 135° to the X axis. As there are a large number of cracks, it would be unsuitable to infer the crack distribution throughout the whole sample using only one micrograph. Sample 5_800_B (b) showing both cracking and LOF defects.

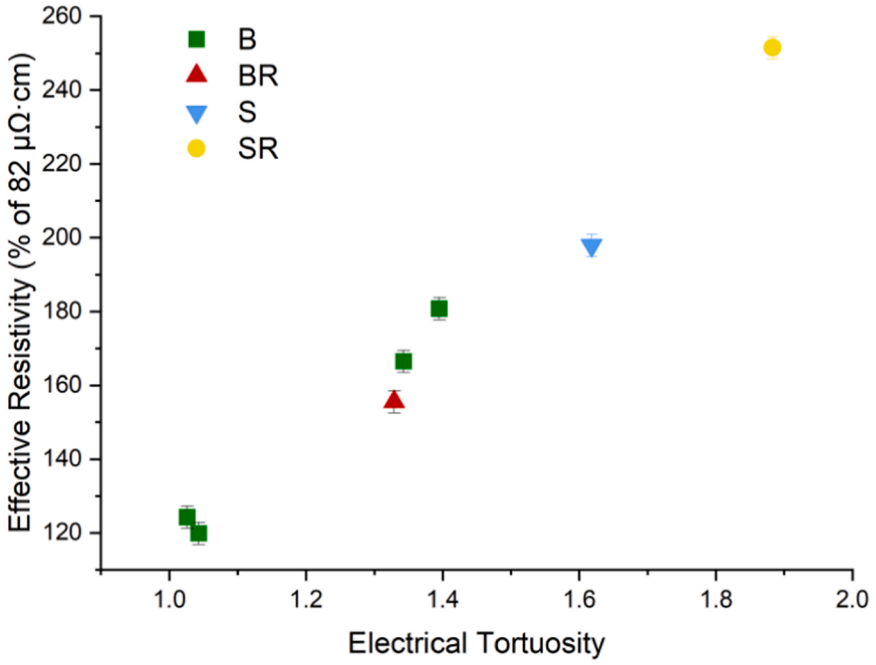

Fig. 7. The electrical tortuosity calculated from the XCT data shows approximately a linear relationship, demonstrating that the scan strategy can create more tortuous pathways without increasing the crack density, as the sample with the S scan strategy shows.

the scan strategy, based upon the electric machine design. If the magnetic flux will always run in a single direction, such as the tooth of an axial flux machine, the cracks can be heavily orientated to optimise for one direction, similar to a grain-orientated electrical steel. If the magnetic flux is required to change direction within the material such as in the back iron of a machine, scan strategies can be manipulated to yield an even crack distribution delivering an equal but lower electrical performance in every direction in a manner similar to non grain-orientated electrical steel.

The crack orientation in the XZ plane was similar for all the scan strategies and an example of this for 3_400_B can be seen in Fig. 9d. Fig. 10 shows an optical micrograph of samples for each of the scan strategies, along with histograms of the crack orientation in the XY plane, which differs between samples. The highest anisotropy is observed for the S scan strategy, showing cracks mainly at 90° to the scan direction (X), but also with a number of cracks parallel to the scan direction. Both strategies with a layer rotation (BR, SR) show a lower anisotropy than without (B, S). Depending on the design of the electric machine, an appropriate scan strategy could be used to ensure the cracks are in the orientation that best serves the machine, increasing the electrical tortuosity of the eddy current flow path. The stripe with rotation (SR) sample shows the highest effective resistivity of 250 % of the bulk resistivity at 206 µΩ·cm.

3.3. Investigation of the residual stress and microstructure

Aside from the stochastic cracking within the samples, other factors such as residual stress, grain size and microstructure could have an impact on the effective resistivity. To ensure that the observed behaviours are an outcome of stochastic cracking, investigation into the other aspects is carried out. To test the effect of residual stress and grain size, the samples were annealed at 1150 °C for 1 h, as reported by Garibaldi et al. [10] to give the best magnetic properties. By using this heat treatment, residual stress was relieved, which may increase or decrease effective resistivity, depending on the residual stress profile. The grain size would also increase, reducing grain boundary density, which is expected to result in a decreased effective resistivity. Fig. 11 shows that after heat treatment, the effective resistivity of the majority of samples change by less than 10 %, with most samples displaying a small increase in resistance. Hence both residual stress and grain size/grain boundary density could not account for the magnitude of increase in effective resistivity shown by the samples in the as-built condition, adding further confidence that cracking is the source of the increased effective resistivity. It may be possible that the thermal stress induced in the part

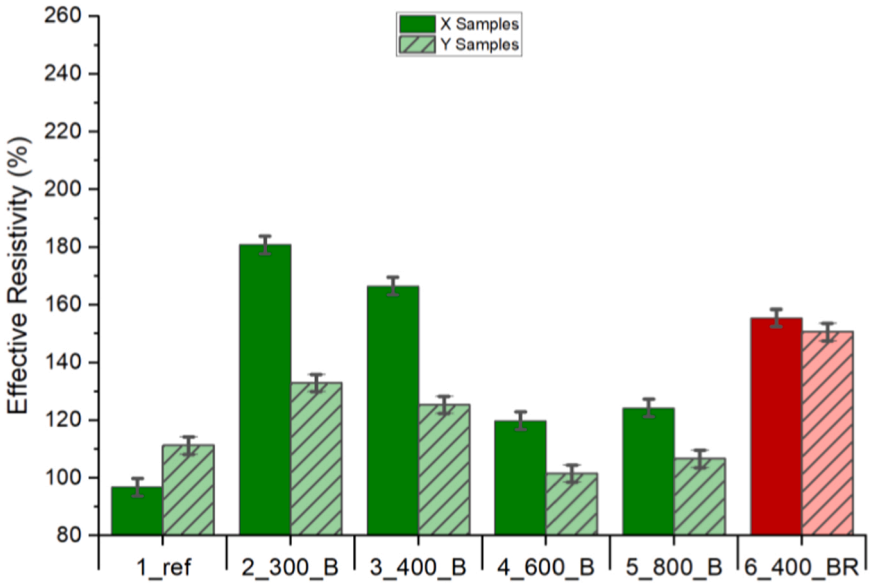

Fig. 8. Difference in effective resistivity between X and Y samples, showing that with a bidirectional scan strategy, the samples have a higher resistance in the X direction, parallel to the scan direction. By introducing a rotation into the scan strategy, the anisotropy is reduced. The reference sample has higher than expected resistivity in the Y sample.

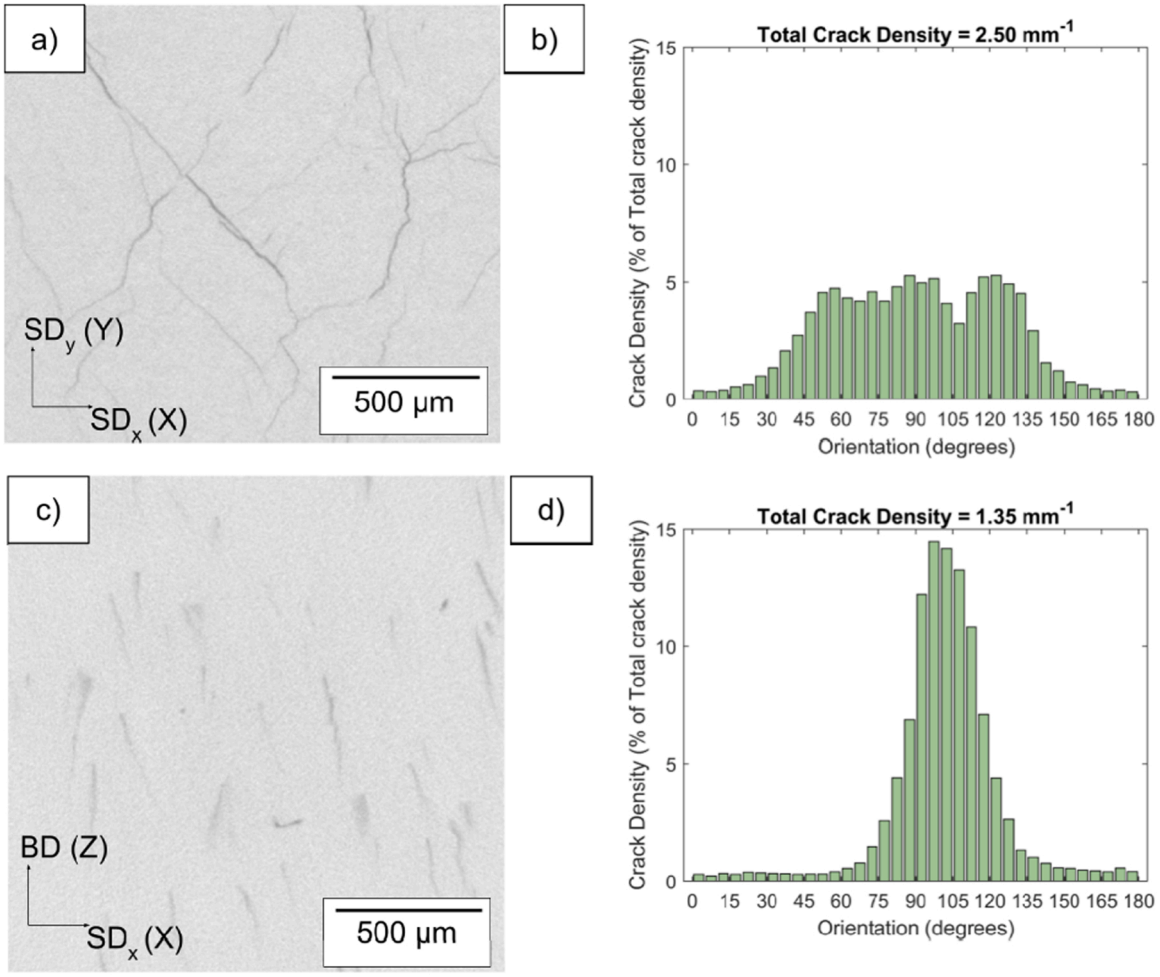

Fig. 9. An example XCT slice from sample 3_400_B in the XY plane (a) and XZ plane (c) and their respective histograms (b, d), showing that in the XY plane there is a strong preference for cracks which are between 45° and 135°, showing a spread centred around 90° (normal to the scan direction), whereas in the XZ plane, cracks have a narrower distribution around 90°.

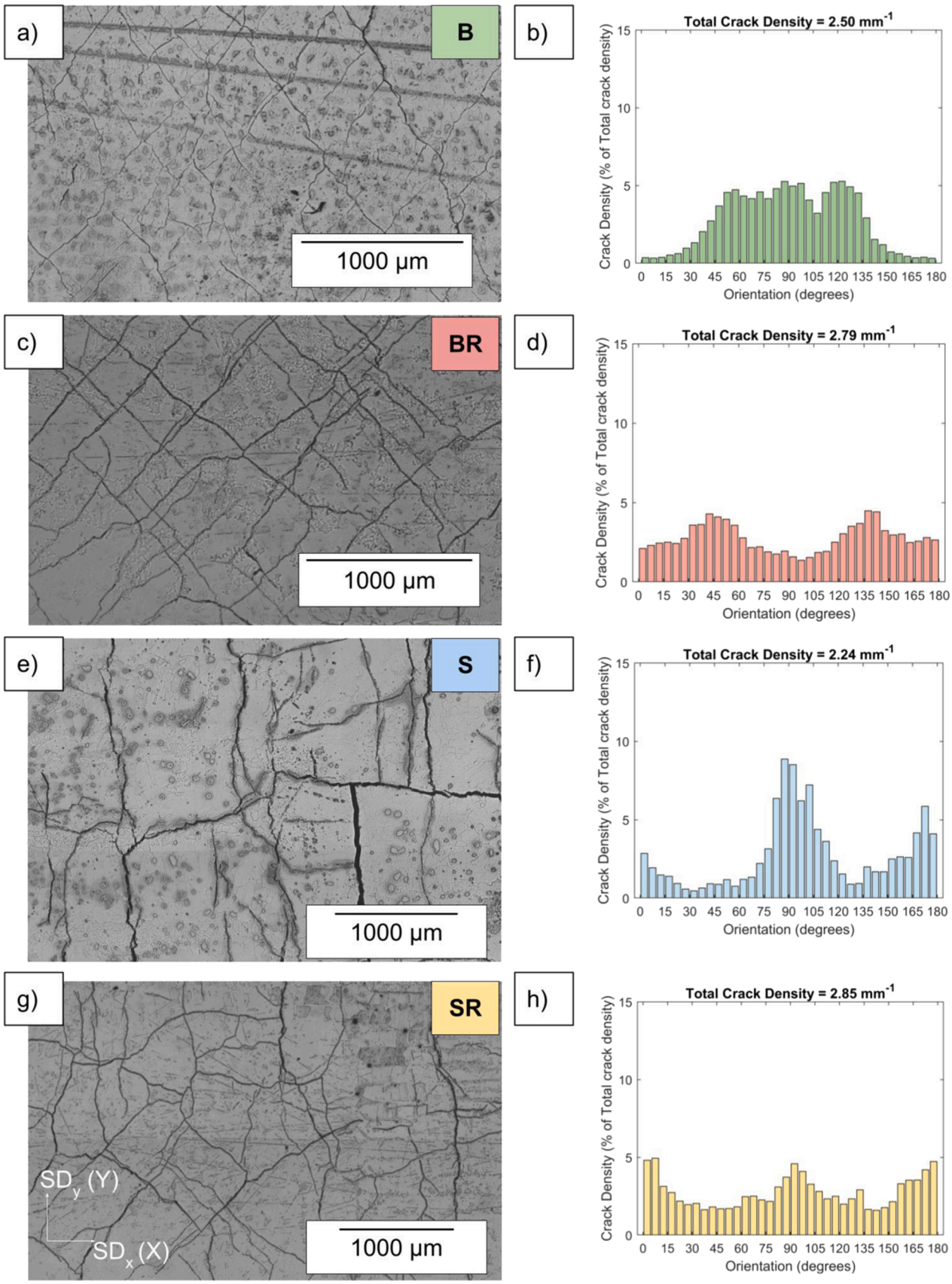

Fig. 10. Optical microscopy images of samples 3_400_B (a), 6_400_BR (c), 7_400_S (e) and 8_400_SR (g) with their respective crack density histograms (b,d,f,h) showing the orientation of the cracks within the sample in the XY plane. 6_400_BR shows cracks mostly in the 45° and 135° directions whereas 8_400_SR shows cracking mostly in either the 0° or 90° direction.

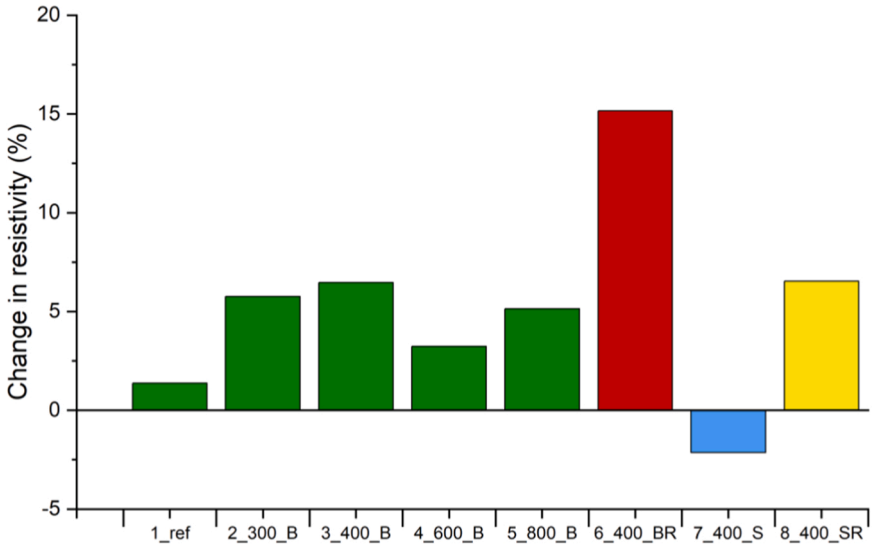

Fig. 11. The percentage change in effective resistivity of each sample post heat-treatment, showing that on average there is less than a 10 % difference between pre and post heat treated samples.

during heat treatment caused cracks to grow, which would increase the effective resistivity.

EBSD analysis was undertaken for all the samples to observe the as-built microstructure. Shown in Fig. 12 is the data for 3_400_B and 8_400_SR as these samples use the same scan speed and power, but exhibit large differences in effective resistivity, 166.5 % and 251.5 % respectively. Sample 8_400_SR shows a common PBF-LB microstructure, with a preferred orientation of the <001> crystallographic direction aligned to the build direction (Z), with elongated grains along this same axis, although the grain size is larger than average with some grains extending over 2 mm. Sample 3_400_B exhibits an unusual microstructure for PBF-LB, with a preference for the <111> texture in relation with the build direction (Z). The texture does show elongated grains up to 0.75 mm long in the build direction (Z), however these are not as large as for 8_400_SR where some grains are > 2 mm long.

3.4. Magnetic characterisation

This work has demonstrated the possibility to increase the effective resistivity of Fe-6.5 wt%Si, by manipulating the laser parameters and scan strategy to introduce stochastic cracking. However, to be used in an EM, electrical resistivity is not the only important parameter, so the impact of the cracks on the other magnetic properties must be investigated. To do this, ring samples were additively manufactured using solid bulk material, a stochastically cracked section and a Hilbert section (similar to that reported by Plotkowski et al. [16], an example cross-section shown in Fig. 15a). The cracked ring was manufactured using parameters 8_400_SR as this showed an average increase in effective resistivity up to 250 %, whilst having a lower anisotropy as shown in Fig. 10h. As shown in Fig. 13, the Hilbert and cracked rings both have a significantly smaller area inside the BH loop, demonstrating lower losses. This is confirmed for the full frequency range tested of 5–1000 Hz (machine limits) in Fig. 14. The shape of the BH loop shows that for the cracked sample, the permeability is reduced to below that of the bulk as the field increases, requiring a higher field to reach the same flux density. The drop in permeability is likely due to cracks or air gaps in the material as these will act as pinning sites for the domain walls and may also make domain rotation more difficult. This reduction in permeability has limited the magnetic measurement to achieving 0.91 T as an upper current limit for the driving coil was reached and the field cannot increase above 5000 A/m. This introduces a preferential bias for the cracked sample, as lower flux density will yield lower losses, however with the current experimental setup, it was not possible to achieve a measurement at 1 T. This will decrease the losses by approximately 10 % as both the hysteresis and eddy current losses are directly proportional to the flux density.

The knee point of the cracked ring appears at a lower flux density than that of the bulk material, this is an issue for EM design, as this would require a higher field to get an equivalent flux density. Heat treatment could improve the permeability as shown by Garibaldi et al. [10], though it may not be possible to achieve the same value as the bulk material due to the extra material defects. The stacking factor of the cracked sections is > 97 %, which is much higher than that of the Hilbert section (83.5 %) as shown in Fig. 15, and likely to remain higher than any cross-sectional design due to the small width of the cracks (< 10 μm) compared to the minimum width of a designed air gap, (> 50 μm). Further to this, cracks provide electrical insulation without any shorting as there will be no contact between the cracked surfaces. This is unlike the designed cross-sections, where surface roughness means that there is often unwanted shorting between areas which should be electrically isolated. Having a higher stacking factor is another enabler to reducing machine size. However, as the cracking is stochastic, there may be higher variability between samples and in order to quantify this variability in the defect population a larger data set would be needed, which falls outside of the scope of this initial study. The number of cracks detected by the XCT and analysed was 20,000–80,000 for a sample only approximately 2 × 2 × 2 mm, hence for the full sample of 25 × 25 × 5 mm it is possible that there are sufficient cracks for the material performance to be predicted statistically. The number of cracks is overstated as the cracks will be counted multiple times (once per slice) due to the nature of the analyse, but this systematic error is accounted for throughout the paper by using crack density.

The cracked samples exhibit lower losses, and a higher stacking factor than the Hilbert cross-section, however, superior loss performance has been obtained by Plotkowski et al. [16] for the Hilbert cross-section, when using a one dimensional flux path. Furthermore, the volume and orientation of cracks will be dependent upon the part geometry, as this will change the thermal conditions in the build. The residual stress is correlated to the hatch length and cross-sectional area [29], if the cross-section is changing, the residual stress will also vary. As this paper shows, a striped scan strategy could be implemented whilst still maintaining a high level of cracking, which is a potential solution to this as any cross-section can be broken down into a number of uniform width stripes. Furthermore, the complex geometries found in EM make it

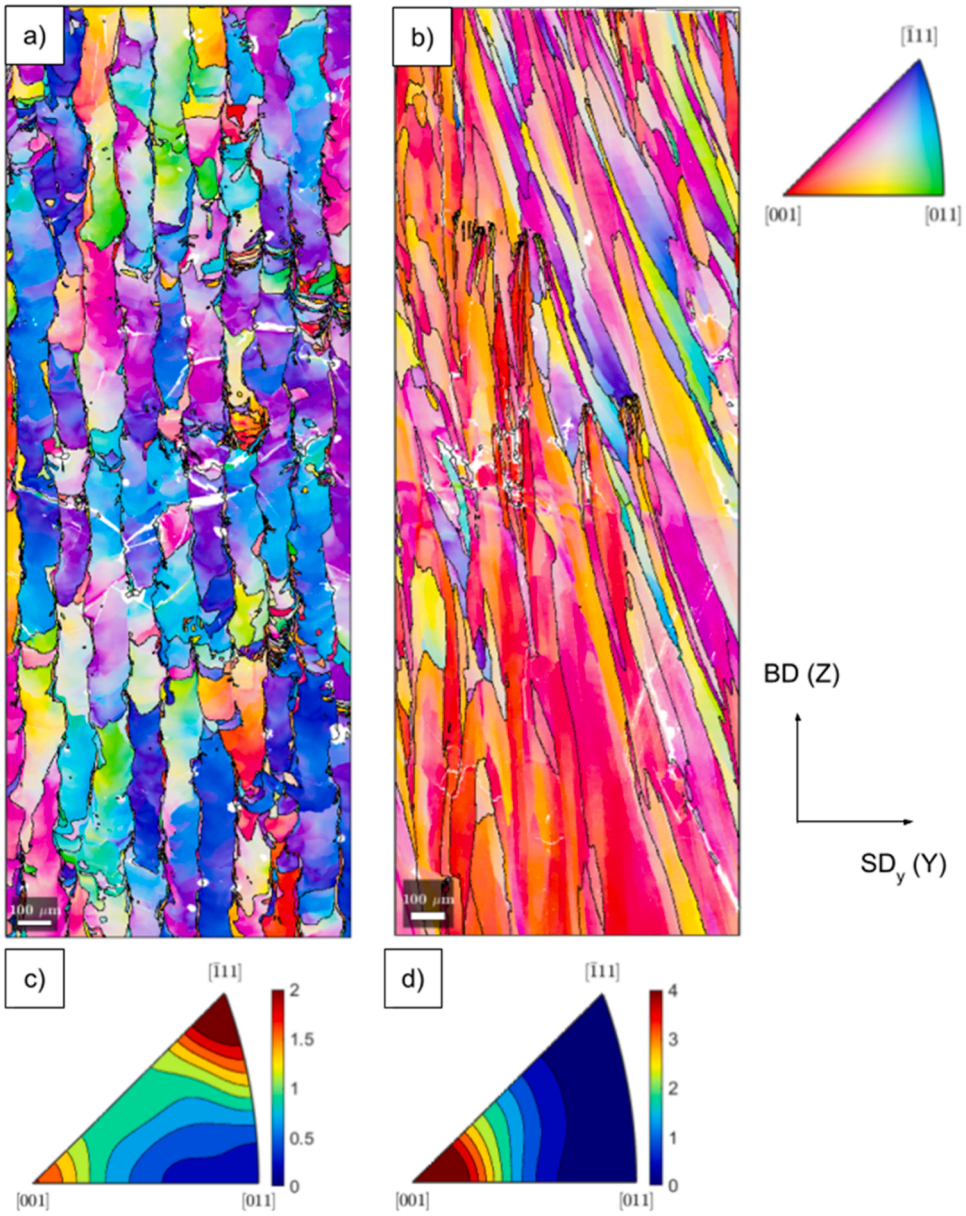

Fig. 12. YZ view of EBSD data showing orientation maps for samples 3_400_B (a) and 8_400_SR (b) and pole figures respectively (c,d). The grain orientation is plotted with respect to the XY plane, showing that 3_400_B has a <111> texture in the build direction (Z), whereas 8_400_SR has a stronger <001> texture in the build direction (Z).

very difficult to characterise the material or magnetic properties of a stochastically cracked component in an actual machine.

Most tests to understand material properties require standard test sample geometries. If one were to use the same parameters to create a small magnetic test ring with a 5 mm cross-section and a stator with a cross-section of 20 mm, it is likely that there would be a difference in crack density and/or orientation, and hence magnetic properties between the two parts. Additionally, there would also be a need to model this magnetic behaviour, otherwise components would have to be made by trial and error by manufacturing components and testing their properties. Models that are able to understand this behaviour are computationally expensive, and are generally limited to a small volume which would not allow a good understanding of the macro-scale behaviour. With further understanding of the underlying process simpler models may be able to be used to aid design.

Electrical resistivity was physically characterised, and electrical tortuosity calculated based on the XCT data in this study. In both cases these measures use a linear current, whereas eddy currents are generally circulating around a cross-section, with a non-uniform amplitude depending on the spatial position. The magnitude of eddy currents is proportional to the material resistivity; therefore, this is not expected to have a significant impact on the results. Utilising the electrical tortuosity calculations, it would be possible to define a circuit path and measure the tortuosity around this path, although to the authors' knowledge, no software currently has this capability. Further to this, the electrical tortuosity calculations are based on geotechnical work, with a solid non-conducting phase which is often a type of rock, and a liquid conducting phase filling the pore space. This is the opposite to the samples analysed in this study where the solid is the conducting phase. For our samples the tortuosity was between 1 and 2, which is relatively low, whereas most work validating these models use higher tortuosity values. The data in this study shows a good correlation between the measured effective resistivity values and the calculated electrical tortuosity, however as this is not a standard use case for this software more validation work would

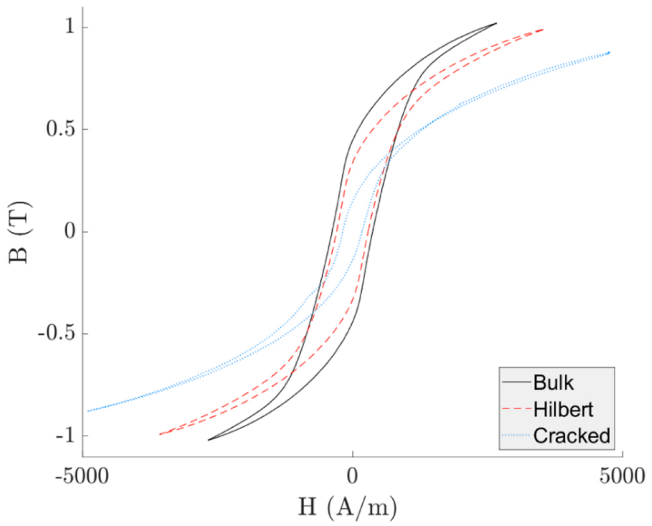

Fig. 13. BH loops of bulk, cracked and Hilbert rings at 50 Hz, 1 T. The Hilbert ring shows lower losses than bulk (area), and the cracked section shows lower losses than both of the other samples. For both the cracked and Hilbert samples, the permeability (gradient) is reduced when compared to the bulk, especially after the knee point in the loop. It is noted that the cracked sample did not achieve 1 T, instead reaching 0.91 T due to reaching a current limit in the driving coil.

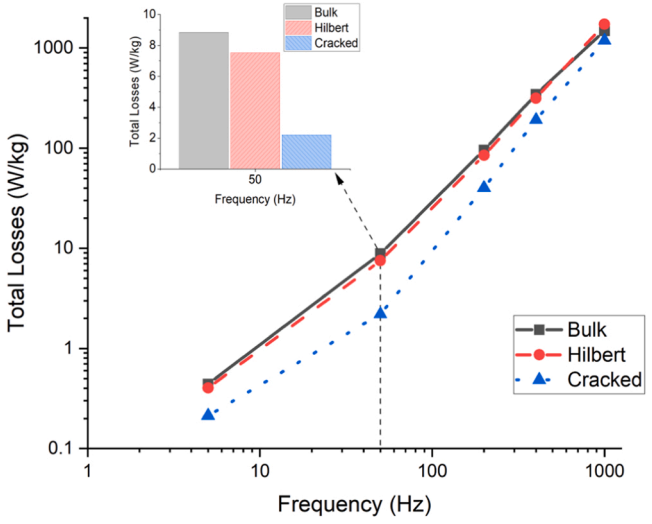

Fig. 14. Loss behaviour of bulk, Hilbert and cracked samples at 1 T, showing that the Hilbert section provides an improvement over bulk, however the cracked ring yields lower losses through the whole frequency range tested than both the other samples. It is noted that the cracked sample did not achieve 1 T, instead reaching 0.91 T due to reaching a current limit in the driving coil.

be needed to confirm its applicability.

The mechanical properties of the stochastically cracked samples have not yet been analysed but are assumed to be inferior to the bulk material and depending upon loading conditions, may also be lower than that of any designed cross-sections such as the Hilbert pattern. Due to extensive cracking, it may not be possible to use stochastic cracking to reduce losses in the rotor of an EM due to the high centrifugal loading; however, the stator has relatively low mechanical requirements and so this methodology should be applicable in this case. The fatigue behaviour through repeated magnetisation and thermal loading would also need to be well understood before this method could be used, as there are concerns that the cracks may propagate and cause the loss of structural integrity. As Fe-6.5 wt%Si has a very low magnetostriction yielding low stresses through the magnetisation cycle, it is likely the best composition to use, however cyclic thermal loading will cause expansion and contraction of the material, which may lead to crack growth and failure. That said, all the samples in the current work possess sufficient structural integrity to handle and process.

The directionality of cracks may be beneficial for EM design, by aligning the cracks parallel to the flux direction this will give the highest resistivity in the plane in which eddy currents would circulate, whilst causing the least disruption to the magnetic flux. An Epstein frame style test could be used to quantify the benefit of this anisotropy, by aligning the cracks along the legs of the Epstein frame to give the highest performance. The design flexibility of the AM process allows for alteration to the scan strategy and laser parameters in different areas of a component, meaning that at every point in the stator, the cracks could run parallel with the magnetic flux, even when using a complex 3D flux path.

The loss behaviour of the stochastically cracked parts is comparable to other materials in production and industrial use today. As shown in Table 3, the losses are lower than both an SMC and a relatively thick low-silicon steel lamination, however thin high-silicon steel laminations still outperform the material characterised in this study. It has been demonstrated, in this study, that it is possible to process material with 3D flux paths, with losses below that of traditionally manufactured Fe-3 wt%Si electrical steel laminations. By directly manufacturing the stator via AM there will also be a reduction in component count, assembly time and cost when compared to a laminated electrical steel stator. This methodology could enable novel electric machine architectures which capitalise on this geometrical freedom to give performance benefits which have been unfeasible with laminations or SMC.

4. Conclusion

In this paper, the ability to manipulate the nature of stochastic cracking during additive manufacturing of Fe-6.5 wt%Si, a high silicon electrical steel, has been demonstrated. It is shown that by reducing the scan speed, the crack density within the material increases, and that by changing the scan strategy the orientation of the cracks can be influenced. By cracking the material using this methodology, an increase in effective electrical resistance up to 206 μΩ·cm, 250% of the expected bulk resistance has been observed in sample 8_400_SR when using a stripe with rotation (SR) scan strategy with a scan speed of 400 mm/s. The total AC losses for this sample at 50 Hz, 1 T are 2.2 W/kg, which shows a reduction in losses to below that of a cross-section with air gaps, such as the Hilbert section (6.8 W/kg, 50 Hz, 1 T), which was purposefully designed to reduce eddy currents. The cracked material shows a higher stacking factor of > 97 %, compared to only 83.5 % for the Hilbert section.

The ability to orient the cracks parallel to the flux path allows for spatial grading to ensure the cracks are always orientated to increase the resistance in the plane in which eddy currents circulate. It is also possible to correlate electrical tortuosity calculated from XCT data with the measured effective resistivity. With low losses and a high stacking factor, stochastic cracking is a promising solution to implementing AM processed soft magnetic material into the stator of an EM, enabling a 3D magnetic flux path with low losses.

CRediT authorship contribution statement

Ria L. Mitchell: Methodology, Data curation. **Geraint W Jewell:** Resources, Methodology, Formal analysis, Data curation. **Alexander Goodall:** Writing – original draft, Methodology, Investigation, Formal analysis, Data curation, Conceptualization. **Lova Chechik:** Writing – review & editing, Software. **Iain Todd:** Writing – review & editing, Visualization, Supervision, Methodology, Funding acquisition, Formal analysis, Data curation.

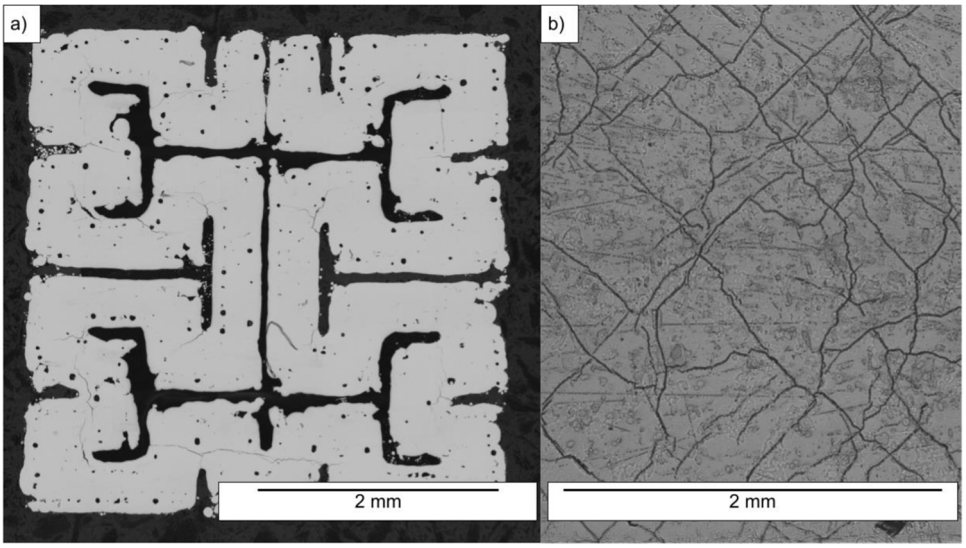

Fig. 15. Micrographs of cross-sections of a Hilbert style pattern (a) with a stacking factor of 83.5 % and a cracked section (b) using parameters 6_400_BR with a stacking factor of 97 %, showing that the cracked section can yield a much higher stacking factor whilst still having lower losses. The Hilbert section has some porosity as the parameters used were optimised for bulk sections, rather than thin walls.

Table 3
Loss behaviour of various materials at 50 Hz and 1 T.

Material	Stochastic cracked 6.5 wt %Si (this study)	AncorLam SMC [30]	JFE 65JN1600 3 wt%Si lamination 0.65 mm [31]	JNEX-Core 6.5 wt%Si lamination 0.1 mm [32]
Losses @ 50 Hz 1 T (W/kg)	2.2	9.0	7.1	0.5

Declaration of Competing Interest

The authors declare that they have no known competing financial interests or personal relationships that could have appeared to influence the work reported in this paper.

Data Availability

Data will be made available on request.

Acknowledgements

We wish to acknowledge the Henry Royce Institute for Advanced Materials, funded through EPSRC Grants EP/R00661X/1, EP/S019367/1, EP/P02470X/1 and EP/P025285/1, for access to the AconityMINI at The University of Sheffield. We also acknowledge Sheffield Tomography Centre and University of Sheffield funding from EPSRC (EP/T006390/1) for use of the Zeiss Xradia 620 Versa X-ray microscope. We also acknowledge Professor Geraint Jewell and Georgios Yiannakou in the Department of Electronic and Electrical Engineering at the University of Sheffield for access to and training on the AMH1K Permeameter by Laboratorio Elettrofisico. For the purpose of open access, the author has applied a Creative Commons Attribution (CC BY) licence to any Author Accepted Manuscript version arising.

Declaration of competing interest

None.

References

[1] J. Zhu, H. Zhou, C. Wang, L. Zhou, S. Yuan, W. Zhang, A review of topology optimization for additive manufacturing: status and challenges, Chin. J. Aeronaut. 34 (2021) 91–110, https://doi.org/10.1016/j.cja.2020.09.020.
[2] C. Emmelmann, D. Herzog, J. Kranz, 10 – design for laser additive manufacturing, in: M. Brandt (Ed.), Laser Addit. Manuf., Woodhead Publishing, 2017, pp. 259–279, https://doi.org/10.1016/B978-0-08-100433-3.00010-5.
[3] M. Garibaldi, I. Ashcroft, M. Simonelli, R. Hague, Metallurgy of high-silicon steel parts produced using selective laser melting, Acta Mater. 110 (2016) 207–216, https://doi.org/10.1016/j.actamat.2016.03.037.
[4] R. Singh, P.D. Lee, R.J. Dashwood, T.C. Lindley, Titanium foams for biomedical applications: a review, Mater. Technol. 25 (2010) 127–136, https://doi.org/10.1179/175355510×12744412709403.
[5] B. Zhang, N.-E. Feneche, L. Zhu, H. Liao, C. Coddet, Studies of magnetic properties of permalloy (Fe–30 %Ni) prepared by SLM technology, J. Magn. Magn. Mater. 324 (2012) 495–500, https://doi.org/10.1016/j.jmmm.2011.08.030.
[6] A.K. Mazeeva, M.V. Staritsyn, V.V. Bobyr, S.A. Manninen, P.A. Kuznetsov, V. N. Klimov, Magnetic properties of Fe–Ni permalloy produced by selective laser melting, J. Alloy. Compd. 814 (2020), 152315, https://doi.org/10.1016/j.jallcom.2019.152315.
[7] C.V. Mikler, V. Chaudhary, T. Borkar, V. Soni, D. Jaeger, X. Chen, et al., Laser additive manufacturing of magnetic materials, JOM 69 (2017) 532–543, https://doi.org/10.1007/s11837-017-2257-2.
[8] X. Yang, J. Liu, X. Cui, G. Jin, Z. Liu, Y. Chen, et al., Effect of remelting on microstructure and magnetic properties of Fe-Co-based alloys produced by laser additive manufacturing, J. Phys. Chem. Solids 130 (2019) 210–216, https://doi.org/10.1016/j.jpcs.2019.03.001.
[9] T. Riipinen, S. Metsä-Kortelainen, T. Lindroos, J. Keränen, A. Manninen, J. Pippuri-Mäkeläinen, Properties of soft magnetic Fe-Co-V alloy produced by laser powder bed fusion, Rapid Prototyp. J. 25 (2019) 699–707, https://doi.org/10.1108/RPJ-06-2018-0136.
[10] M. Garibaldi, I. Ashcroft, J.N. Lemke, M. Simonelli, R. Hague, Effect of annealing on the microstructure and magnetic properties of soft magnetic Fe-Si produced via laser additive manufacturing, Scr. Mater. 142 (2018) 121–125, https://doi.org/10.1016/j.scriptamat.2017.08.042.
[11] M. Garibaldi, I. Ashcroft, N. Hillier, S.A.C. Harmon, R. Hague, Relationship between laser energy input, microstructures and magnetic properties of selective laser melted Fe-6.9 wt% Si soft magnets, Mater. Charact. 143 (2018) 144–151, https://doi.org/10.1016/j.matchar.2018.01.016.
[12] H. Tiismus, A. Kallaste, A. Rassölkin, T. Vaimann, Preliminary analysis of soft magnetic material properties for additive manufacturing of electrical machines, Key Eng. Mater. 799 KEM (2019) 270–275, https://doi.org/10.4028/www.scientific.net/KEM.799.270.
[13] A. Krings, M. Cossale, A. Tenconi, J. Soulard, A. Cavagnino, A. Boglietti, Magnetic materials used in electrical machines: a comparison and selection guide for early machine design, IEEE Ind. Appl. Mag. 23 (2017) 21–28, https://doi.org/10.1109/MIAS.2016.2600721.
[14] G. Ouyang, X. Chen, Y. Liang, C. Macziewski, J. Cui, Review of Fe-6.5 wt%Si high silicon steel—a promising soft magnetic material for sub-kHz application, J. Magn. Magn. Mater. 481 (2019) 234–250, https://doi.org/10.1016/j.jmmm.2019.02.089.

[15] M. Garibaldi, C. Gerada, I. Ashcroft, R. Hague, H. Morvan, The Impact of Additive Manufacturing on the Development of Electrical Machines for MEA Applications: A Feasibility Study, MEA2015 More Electr. Aircr., Toulouse, France, 2015.
[16] A. Plotkowski, J. Pries, F. List, P. Nandwana, B. Stump, K. Carver, et al., Influence of scan pattern and geometry on the microstructure and soft-magnetic performance of additively manufactured Fe-Si, Addit. Manuf. 29 (2019), 100781, https://doi.org/10.1016/j.addma.2019.100781.
[17] D. Goll, D. Schuller, G. Martinek, T. Kunert, J. Schurr, C. Sinz, et al., Additive manufacturing of soft magnetic materials and components, Addit. Manuf. 27 (2019) 428–439, https://doi.org/10.1016/j.addma.2019.02.021.
[18] B. Koo, M.-S. Jang, Y.G. Nam, S. Yang, J. Yu, Y.H. Park, et al., Structurally-layered soft magnetic Fe-Si components with surface insulation prepared by shell-shaping selective laser melting, Appl. Surf. Sci. 553 (2021), 149510, https://doi.org/10.1016/j.apsusc.2021.149510.
[19] C.A. Schneider, W.S. Rasband, K.W. Eliceiri, NIH Image to ImageJ: 25 years of image analysis, Nat. Methods 9 (2012) 671–675, https://doi.org/10.1038/nmeth.2089.
[20] G.W. Zack, W.E. Rogers, S.A. Latt, Automatic measurement of sister chromatid exchange frequency, J. Histochem. Cytochem. 25 (1977) 741–753, https://doi.org/10.1177/25.7.70454.
[21] Mathworks, Matlab R2020a, 2020.
[22] B. Ghanbarian, A.G. Hunt, R.P. Ewing, M. Sahimi, Tortuosity in porous media: a critical review, Soil Sci. Soc. Am. J. 77 (2013) 1461–1477, https://doi.org/10.2136/sssaj2012.0435.
[23] M. Matyka, Z. Koza, How to calculate tortuosity easily? AIP Conf. Proc. 1453 (2012) 17–22, https://doi.org/10.1063/1.4711147.
[24] ThermoFisher Scientific, Avizo 3D, n.d.
[25] ThermoFisher Scientific, User's Guide Avizo Software 2019, 2019.
[26] ThermoFisher Scientific, Simulation-Based Tortuosity Estimation of Porous Media, 2019.
[27] BSI, BS60404-6-2018 Methods of measurement of the magnetic properties of magnetically soft metallic and powder materials at frequencies in the range 20 Hz to 100 kHz by the use of ring specimens, 2018.
[28] J.P. Oliveira, T.G. Santos, R.M. Miranda, Revisiting fundamental welding concepts to improve additive manufacturing: from theory to practice, Prog. Mater. Sci. 107 (2020), 100590, https://doi.org/10.1016/j.pmatsci.2019.100590.
[29] P. Mercelis, J. Kruth, Residual stresses in selective laser sintering and selective laser melting, Rapid Prototyp. J. 12 (2006) 254–265, https://doi.org/10.1108/13552540610707013.
[30] Hoeganaes, AncorLam Materials Datasheet, n.d. ⟨https://www.gknpm.com/globalassets/downloads/gkn-hoeganaes/pm-materials/engineered-solutions-for-pm/ancorlam.pdf/⟩, (Accessed 6 July 2022).
[31] JFE Steel Corporation, ELECTRICAL STEEL SHEETS, n.d. ⟨https://www.jfe-steel.co.jp/en/products/electrical/catalog/f1e-001.pdf⟩, (Accessed 6 July 2022).
[32] JFE Steel Corporation, Super core – electrical steel sheets for high-frequency applicatoin, n.d. ⟨https://www.jfe-steel.co.jp/en/products/electrical/catalog/f1e-002.pdf⟩, (Accessed 6 July 2022).